Individual and collective effects of titanium carbides and multi-walled carbon nanotubes on reinforcing the Inconel 625 alloy fabricated by laser powder bed fusion

Siyuan Wei[1,*], Jun Jie Tang[2], Abhinav Jha[3], Kwang Boon Lau[1], Delvin Wuu[1], Verner Soh[1], Qiang Zhu[1], Cheng Cheh Tan[1], Pei Wang[1,*], Dongzhi Chi[1]

1. *Institute of Materials Research and Engineering, Agency for Science, Technology and Research, 138634, Republic of Singapore*
2. *School of Materials Science and Engineering, Nanyang Technological University, 639798, Republic of Singapore*
3. *Department of Management Science and Engineering, Stanford University, CA-94305, USA*

*Corresponding Authors: siyuan_wei@imre.a-star.edu.sg, wangp@imre.a-star.edu.sg,

Abstract

Nano-additives reinforced Inconel 625 alloys were manufactured by laser powder bed fusion (LPBF), consisting of titanium carbide nanoparticles (TiC) and/or nickel-coated multi-walled carbon nanotubes ((Ni)MWCNT). Microstructural characterization revealed that respective structures of TiC and (Ni)MWCNT nano-additives were retained, while the (Ni)MWCNT experienced fragmentation into shorter segments after ball milling and LPBF. Compared to LPBF In625, the reinforced samples showed enhanced ultimate tensile strength, yield strength, and hardness, despite decreased elongation to failure. Nano-additives exert varying effects on the properties of the alloys. Individually, (Ni)MWCNT strengthens the alloy, and TiC plays an insignificant role; collectively, they strengthen the material to a higher degree, via refining the cell size and probably increasing dislocation density.

Keywords: Inconel 625; laser powder bed fusion; mechanical property; titanium carbide; multi-walled carbon nanotubes.

1. Introduction

Incorporating nanoscale particles or other types of additives into the metallic powders during additive manufacturing (AM) process has gained significant popularity, for the following reasons. (I) The nano-additives, which typically possess higher melting points than the matrix, can act as nucleation sites during solidification and contribute to grain refinement and elimination of cracking [1,2]. (ii) The reinforced alloys, commonly known as metal matrix composites (MMCs), exhibit superior mechanical properties compared to the matrix, due to the strengthening effect of the nano-additives [3,4]. (iii) Fabricating MMC using AM is more flexible and efficient than the conventional methods, as multiple steps of (post)processing are not mandatory.

Similar to conventional MMCs, ceramic particles (e.g., titanium carbide (TiC), silicon carbide (SiC), and titanium borides (TiB or TiB_2), are the most common choices in AM process, due to their high strength, thermal stability, and good compatibility with the metal matrix. For example, the effectiveness of TiC nanoparticles on modulating the microstructure and mechanical properties have been revealed in various types of alloys, e.g., steels [3,5], Ni-based superalloys [6,7], and Al alloys [8,9]. Except for the conventional reinforcements, another promising candidate is carbon nanotube (CNT), due to its high strength, light weight, and thermal/electrical conductivity [4,10-12]. The major challenges in fabricating CNT-containing MMCs using AM are (i) the van der Waals force between the CNT surfaces, which tends to cause agglomeration of CNTs, and (ii) the disintegration of CNT upon scanning of the high-energy beam. It has been reported that using Ni-coated multi-walled CNTs ((Ni)MWCNT) can effectively improve the stability and the level of dispersion during the laser powder bed fusion (LPBF) process [4,10].

Despite the active exploration of constructing MMCs through both conventional methods and AM, a significant bottleneck persists. While a large quantity of reinforcements can achieve high strength, it often comes at the cost of a drastic decrease in ductility and toughness. Conversely, employing a limited number of reinforcements typically results in only marginal improvements in the material's mechanical properties. In conventional MMCs, one promising approach is to add a variety of reinforcements into metal matrix to achieve their collective effects [13,14], which is known as hybrid reinforcing. For instance, enhanced friction behavior at room and elevated temperatures is seen in hybrid Al-SiC-CNT composites, compared to that of Al-SiC [15]. In hybrid composites, the reinforcements can act individually or engage in interaction with each other. This interaction can occur through modifications in distribution or bonding, ultimately contributing to a collective achievement of superior performance [13]. In additive manufacturing, the hybrid composites are yet to be widely explored. Moreover, the rapid solidification and unique structures, e.g., melt pools and cellular structures, would result in distinct structures and mechanical properties. Therefore, it is of great importance to investigate the collective effects of additives/reinforcements in the AM alloys.

In this study, TiC and (Ni)MWCNT nano-additives are incorporated into In625 alloy to study their individual and collective effects. Four types of alloys, i.e., In625, In625-(Ni)MWCNT, In625-TiC, and In625-(Ni)MWCNNT-TiC were fabricated and their microstructure and mechanical properties were carefully studied. The morphology and structure of the nano-additives in the fabricated samples were characterized and their effects were discussed.

2. Experiment

Spherical powders of In625 with the compositions shown in Table 1 were obtained from LPW Technology. Using sieve analysis, according to ASTM B214 Standard, the D10, D50, and D90 of the In625 powders are measured to be 15.3, 22.8, and 44.3 μm, respectively. A powder size distribution map, obtained using laser diffraction method, was further plotted in Figure 1(a). Two types of nano-additives, (Ni)MWCNT, supplied by US Research Nanomaterial Inc. and TiC, supplied by Sigma-Aldrilch, were utilized. Further details of these additives are given in Table 2. The IN625 powder were added with either (i) 0.25 wt.% (Ni)MWCNT, or (ii) 0.25 wt.% TiC, or (iii) 0.125wt.% (Ni)MWCNT + 0.125 wt.% TiC. The mixed powders were ball milled for a total duration of 580 min with a 20 min interval every 20 min. The interruptions in milling were implemented to allow the milling bowl to cool down and prevent heat accumulation. The powders mixtures were subsequently sieved and dried for 12 h at 100 °C before use.

Table 1. Chemical compositions of the Inconel 625 alloy powders (wt.%).

Ni	Cr	Mo	Fe	Nb	Co	Cu	Mn	Si	Al	Ti	C	Ta	P	S
Bal.	20.0-23.0	8.0-10.0	5.0 max	3.15-4.15	1.0 max	0.5 max	0.5 max	0.5 max	0.4 max	0.4 max	0.1 max	0.05 max	0.015 max	0.015 max

Table 2. Material specification of nickel-coated multi-walled carbon nanotube.

Purity (wt.%)	98
Content of nickel (wt.%)	> 60
Content of CNTs (wt.%)	> 38
Outside diameter (nm)	20~30
Inside diameter (nm)	5~10
Length (μm)	10~30
Density (g/cm^3)	0.27

A 250HL machine from SLM Solutions (with laser spot size of 80 μm and wavelength of 1046 nm) was utilized for LPBF. After the initial process parameter optimization that minimizes porosity and eliminates cracking, the following parameter combination was utilized all the different compositions examined in this work: laser power = 360 W, layer thickness = 50 μm, scanning speed = 400 mm/s, and hatch spacing = 125 μm. A chessboard scanning strategy with an island size of 1 × 1 mm^2 was utilized, as schematically shown in Figure 1. Coupons of 110×10×20 mm^3 were fabricated and wire-cut from the 316L steel substrate for further characterization and testing. All the samples exhibit no cracking and porosity of less than 1%.

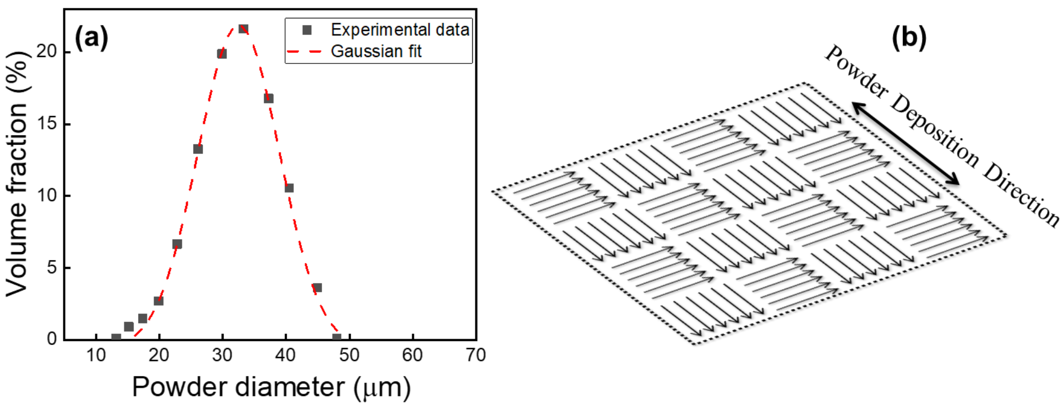

Figure 1. (a) Powder size distribution map obtained using laser diffraction method. (b) Schematic diagram of the chessboard scanning strategy.

An X-ray diffractor (XRD, Bruker D8) with a Cu X-ray source (wavelength of 0.15418 nm), optical microscope, and JEOL JSM 7600 field emission scanning electron microscope (SEM), equipped with both energy dispersive X-ray spectrometer (EDX) and electron backscatter diffraction (EBSD) detectors, were utilized for microstructural characterization.

The Raman spectroscopy analysis was performed using the WITec Alpha300RS correlative Raman microscopy equipped with a laser system with wavelength of 532 nm and power of 5 mW. A JEOL 2100 transmission electron microscope (TEM) operating at 200 kV was utilized for characterizing the samples that were prepared using a Helios NanoLab 450S focus ion beam (FIB) system. Flat dog-bone shaped specimens (6×2×1 mm^3 in gauge area) were used for tensile testing with a nominal strain rate of 0.5 m/min at room temperature, according to ASTM E8/E8M-13a. At least three repeats were conducted for each condition to ensure the reliability of the results. Vickers hardness testing was performed using 300 g load and 10 s holding time and at least 6 repeats were conducted for each condition.

3. Results and discussion

3.1. Microstructural characterization

Representative morphology of IN625 powders after ball milling with the nano-additives. is shown in Figure 2(a). As seen, the IN625 powders retain their size (~34.9 µm, in range of original 15–45 µm) and spherical shape. Figures 2(b), (c), and (d) demonstrate the successful incorporation of (Ni)MWCNT, TiC and (Ni)MWCNT-TiC onto the IN625 powders, respectively. According to the shape of the nano-additives, stripe-shaped (Ni)MWCNT and TiC spherical particles are marked out using red and yellow arrows, respectively. Note that the SEM images presented here solely aim to showcase the morphological variations observed on the powder surfaces post-mixing. The detailed examination of the nano-additives' existence, morphologies, and distributions will be shown in the subsequent sections.

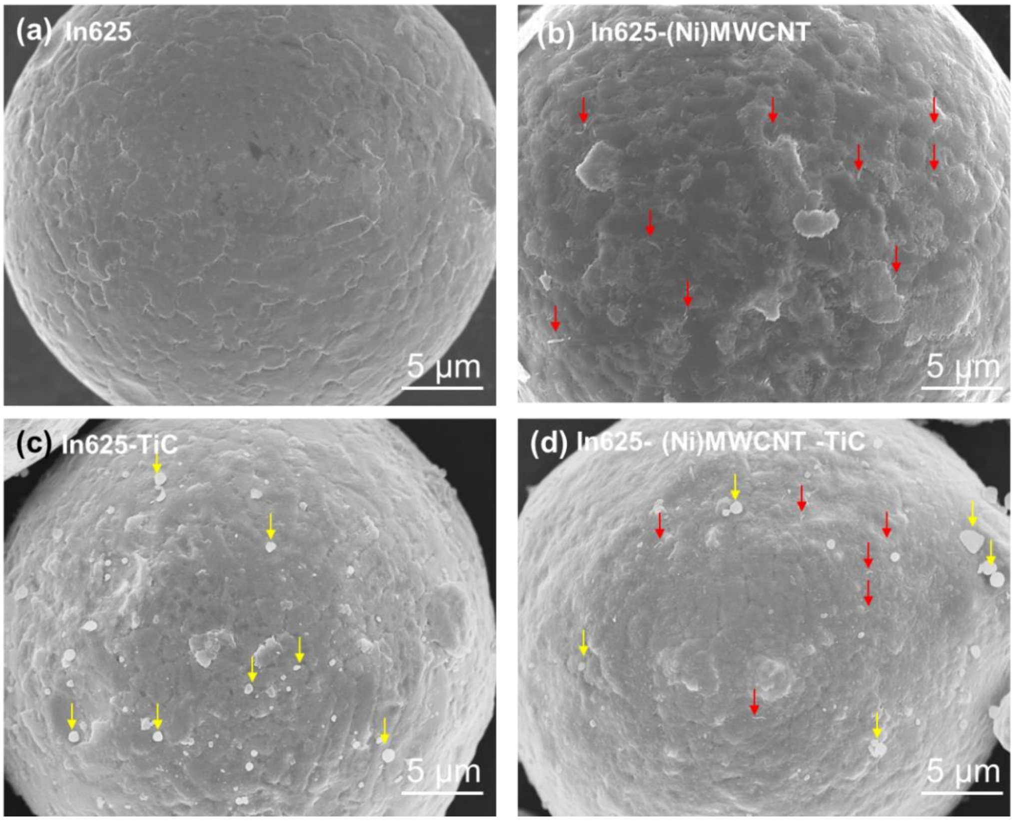

Figure 2. (a) Representative secondary electron images of IN625 powders. Nano-additives attached on the surfaces of IN625 powders in the mixtures of (b) (Ni)MWCNT, (c) TiC, and (d) (Ni)MWCNT-TiC. Red and yellow arrows indicate the (Ni)MWCNT and TiC, respectively.

To study the phase variations, XRD was performed, and the patterns obtained on the IN625 powder and the LPBF In625, IN625-(Ni)MWCNT, IN625-TiC, and IN625-(Ni)MWCNT-TiC alloys are displayed in Figure 3(a). All the samples possess a face centered cubic (FCC) crystal structure. Further analysis reveals that the addition of (Ni)MWCNT leads to the formation of a trace number of carbides, as reflected by the presence of weak peaks in Figure 3(b). Other microstructural phases such as the Laves phase and oxides can also be expected in the as-LPBF IN625 samples [16,17]. The fact that these phases were not detected here could be inferred as they are either small in quantity and/or size.

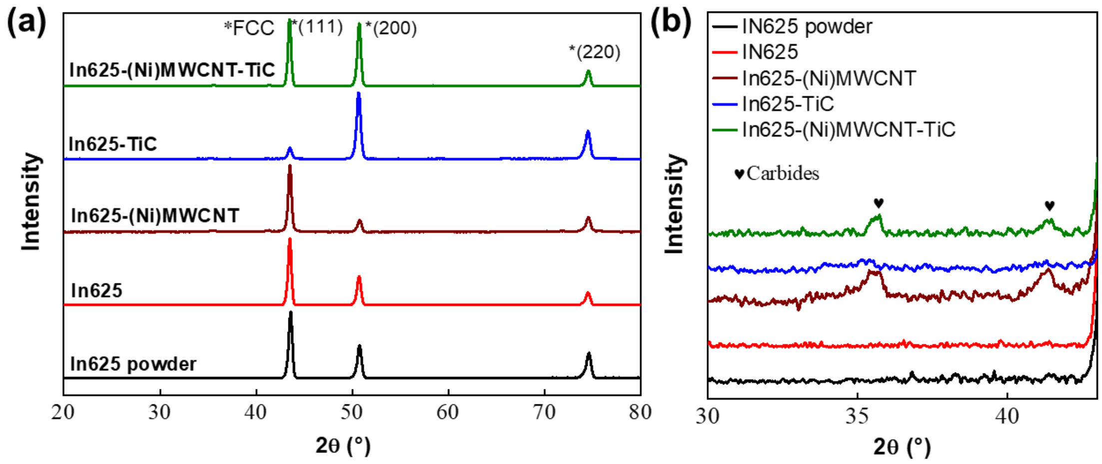

Figure 3. (a) XRD patterns of the In625 powder and LPBF samples; (b) Zoomed-in patterns.

Raman spectroscopy was utilized to confirm the existence and structure of (Ni)MWCNT, as it can detect the information about the crystallite size, clustering of the sp^2 phase, and sp^2-sp^3 hybridization of the CNTs [18]. The results are shown in Figure 4. The observation of the characteristic D and G peaks at 1356 and 1580 cm^{-1}, respectively, indicate the existence of MWCNTs in both IN625+(Ni)MWCNT powder mixtures and as-printed (AP) IN625-(Ni)MWCNT [19].

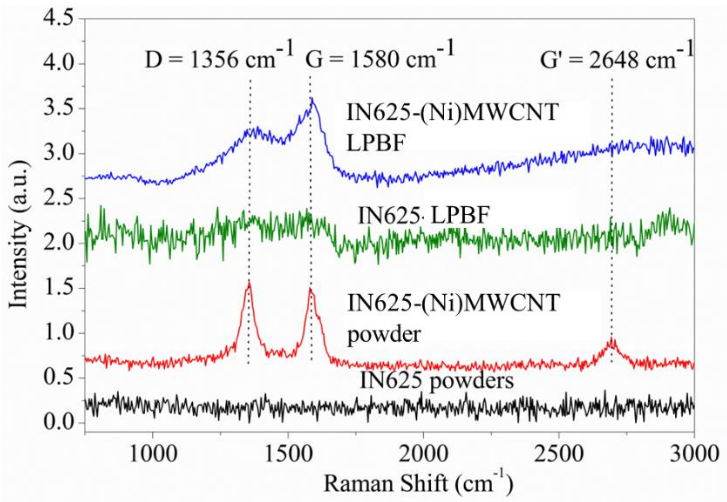

Figure 4. Raman spectroscopy of In625 and In625-(Ni)MWCNT, in both powder and as-printed states.

High resolution TEM and fast Fourier transform (FFT) pattern were further utilized to identify and characterize the nano-additives in the AP samples (IN625-(Ni)MWCNT-TiC).

Most of the TiC particles observed in the samples retain their spherical shape (Figure 5(a)) and have an average diameter of 94.5 nm. The FFT pattern (Figure 5(b)) shows that TiC particle has incoherent interface with the matrix, as evidenced by the misalignment between the (002) planes of TiC and the IN625 matrix. The (Ni)MWCNT is observed to be of ~210 nm in length and ~46.5 nm in width (typical morphology shown in Figure 5(c)). The decrease of length of (Ni)MWCNTs (10–30 μm in the pristine condition, Table 2) can be attributed to the fragmentation that might have occurred during both ball milling and LPBF. It is also interesting to note that (Ni)MWCNT and TiC tend to aggregate, as shown in Figure 5(a).

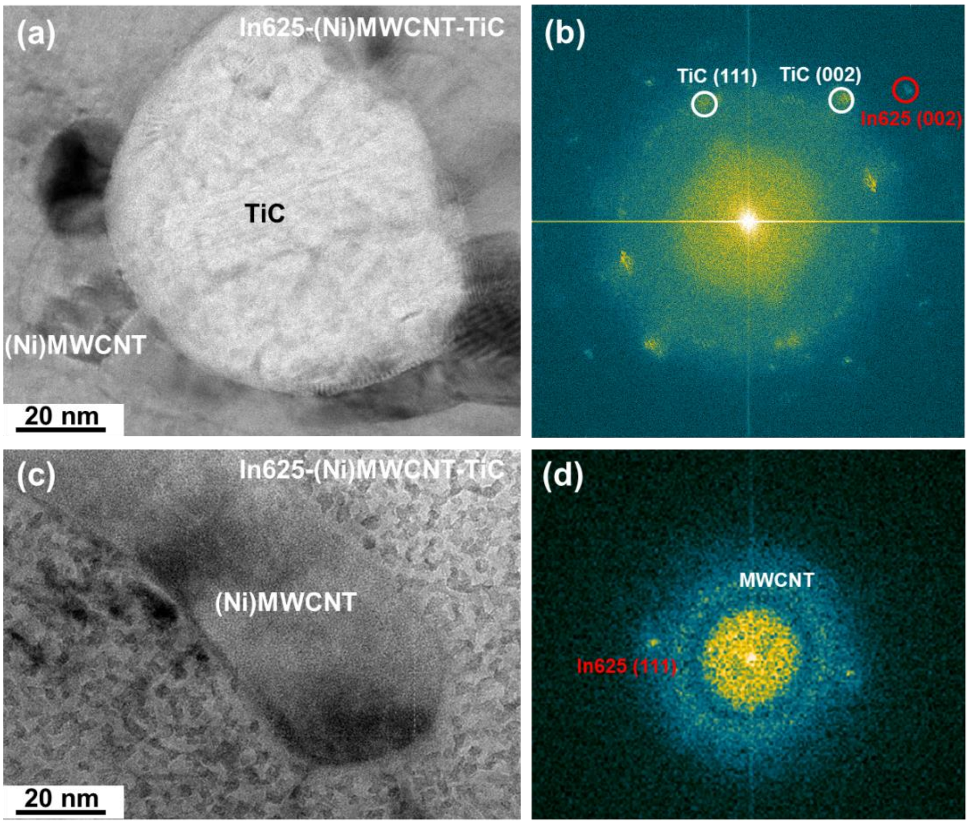

Figure 5. High resolution TEM bright-field images and the corresponding fast Fourier transform pattern (FFT) of nano-additives in In625-(Ni)MWCNT-TiC samples. (a-b) TiC and (c-d) (Ni)MWCNT.

The results of Raman spectroscopy and HRTEM show that (Ni)MWCNT and TiC retain their intrinsic crystal structures after LPBF. SEM characterization was further conducted on the etched samples to study the morphologies of cellular structures—a characteristic of many LPBF alloys [20,21]—and the distribution of nano-additives along them. As shown in Figure 6, the nano-additives are predominantly found near the cellular boundaries, which shows different brightness from the matrix due to the difference in electrical conductivity and charging effect. Nano-additives with high melting points (CNT: 3550 °C, TiC: 3160 °C [22]) are known to act as heterogeneous nucleation sites during solidification [1]; it is not surprising they are preferably located along the cell boundaries, as the cellular structures are essentially primary dendritic arms formed upon solidification.

The average widths of cellular structures in In625-(Ni)MWCNT, In625-TiC, and In625-(Ni)MWCNT-TiC were measured to be ~1.2, 1.3, and 0.7 μm, respectively. It is interesting to note that while the samples with either (Ni)MWCNT or TiC show similar sizes of cellular structures, the two nano-additives collectively exert more significant influence on the cell size. In AM alloys, the cellular structures are essentially primary dendrites without secondaries arms, which is a characteristic feature induced by rapid solidification [21,23]. The formation of cellular structures commonly commences at the boundary of the melt pool and progresses along a path parallel to the maximum heat flow direction, which, in the context of LPBF, aligns perpendicular to the solidifying surface of the melt pool. Figures 6(a) and 6(c) showcase the typical morphology of the cellular structures, which have straight boundaries. However, the cellular structures in In625-(Ni)MWCNT-TiC sample (Figure 6(e)) show tortuous boundaries, indicating their growth during the solidification was interrupted. It is not surprising that nano-additives can act as nucleation sites for the growth of dendrites, but (Ni)MWCNT and TiC collectively result in finer cell size is unexpected. This could be related to the fluid dynamics of the melt pool (susceptive to powder component) [24] as well as cooling rate (due to the varying thermal conductivity of the nano-additives) [25]. To comprehensively address this matter, future investigations, possibly involving thermodynamic and fluid dynamics simulations, will be needed.

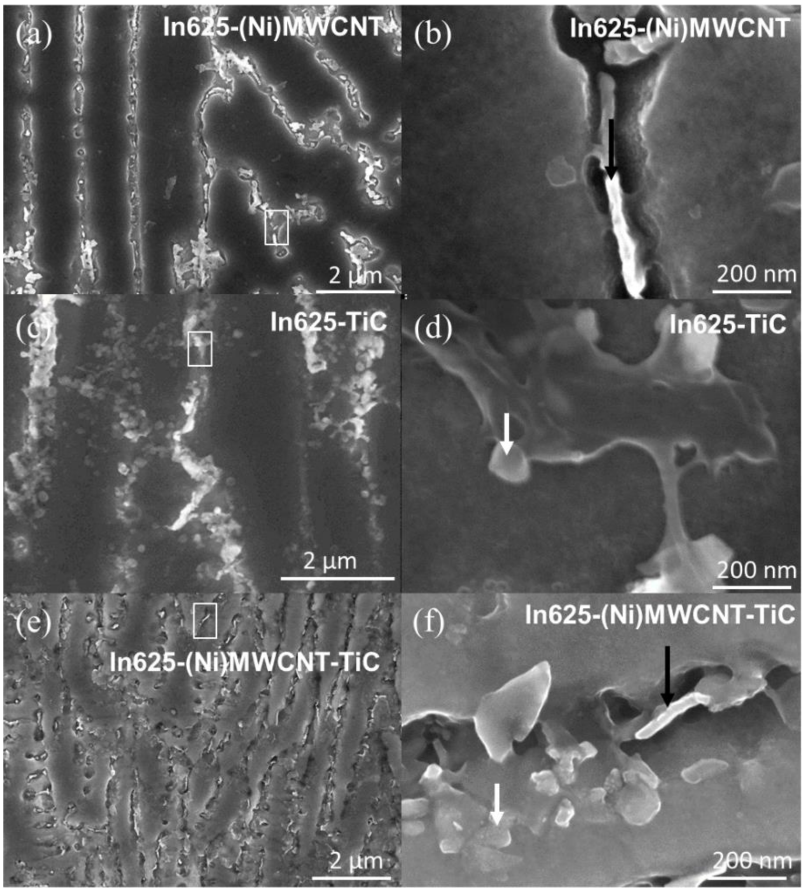

Figure 6. Representative secondary electron images of (a-b) In625-(Ni)MWCNT, (c-d) In625-TiC, and (e-f) In625-(Ni)MWCNT-TiC. Figures (b), (d), and (f) are zoomed-in images of areas highlighted by white lines in figures (a), (c), and (e), respectively. Black and white arrows indicate the (Ni)MWCNT and TiC nano-additives, respectively.

Keep the above information on the structures and morphologies of nano-additives in mind, further microstructural investigation is focused on the grain morphologies. Crystallographic orientation maps of all the four alloys, characterized using EBSD, are shown in Figure 7. (Only FCC phase was detected by EBSD in each sample, due to the small quantity and size of the secondary phases.) Columnar grains with preferred orientations of <001> and <011> are observed in all of them. Such grain morphology is typically expected in the LPBF alloys, due to a relatively smaller energy barrier for the epitaxial growth of the grains [23,26]. Further analysis on the grain size reveals that In625, In625-(Ni)MWCNT, In625-TiC, and In625-(Ni)MWCNT-TiC have average grain sizes (equivalent circular diameter) of 19.2, 17.3, 15.0, and 17.6 µm respectively. The fact that nano-additives in this work only contribute slightly to the grain refinement is in contrast to the phenomenon observed in other systems, where nanoparticles altered the microstructure from columnar to equiaxed, e.g., Al7075+TiB_2 [1], 316L+TiC [3]. This could be attributed to that the number of nano-additives of the current study being low, i.e., 0.25 wt.%. For example, it was reported in the literature that 3 wt.% TiC was incorporated into the 316L austenitic stainless steel induces evident grain refinement [3]. Another phenomenon worth noting is the abrupt change of grain orientation in some localized areas (e.g., left-hand part of Figure 7(c)). This can be understood via the following mechanisms. (i) The ultrafast cooling rate and cyclic heating during LPBF can result in residual stress and localized plastic deformation. (ii) The nano-additives incorporated into the system would remain solid-state during solidification and then impede the continuous plastic deformation, leading to the abrupt change of grain orientation.

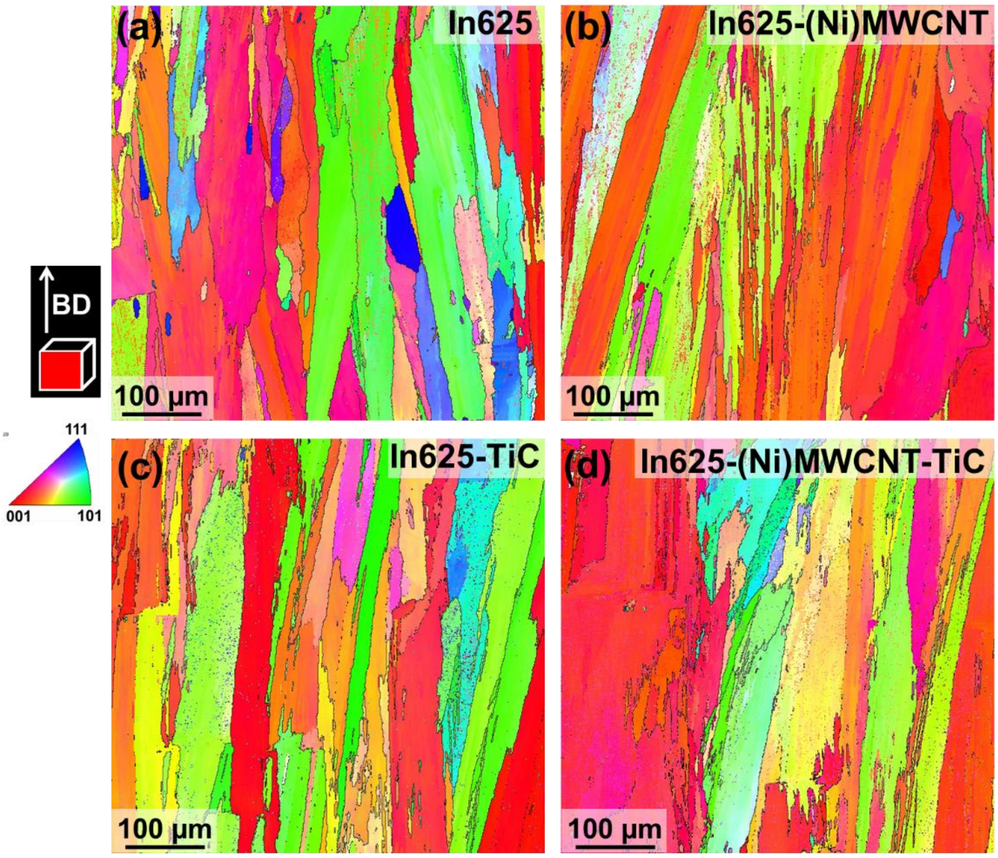

Figure 7. Crystallographic orientation maps of (a) In625, (b) In625-(Ni)MWCNT, (c) In625-TiC, and (d) In625-(Ni)MWCNT-TiC, obtained using EBSD.

3.2. Mechanical properties

To gain insights into the effects of nano-additives on the mechanical behaviors of the In625 alloys, hardness and tensile testing were performed. The average Vickers hardness values obtained from the top and side planes (at least 6 repeat tests were performed for each condition) are shown in Figure 8(a). It is observed that the side planes are harder than the top ones in each sample. The anisotropic nature of hardness can be attributed to two factors (i) the textured columnar grains, where the grain morphology and size differ and (ii) the build height which affects the accumulation of residual stress [21,27]. Importantly, the nano-additives harden the In625 matrix, with the combination of (Ni)MWCNNT + TiC hardening the most. Tensile testing was further conducted to investigate the effect of nano-additives on the mechanical properties. The representative engineering strain-stress plots are shown in Figure 8(b). The nano-additives reduced the ductility significantly—elongation to failure decreased from 33 % to ~20%. While addition of (Ni)MWCNT and (Ni)MWCNT + TiC enhanced the strength (both yield and ultimate tensile strengths), TiC addition did not affect the strengthen evidently. However, when MWCNT and TiC are added together, a synergic effect in strength is noted. The strengthening due to the simultaneous addition of both these phases is higher than the combination of induvial strengthening caused by each of the nano-additives.

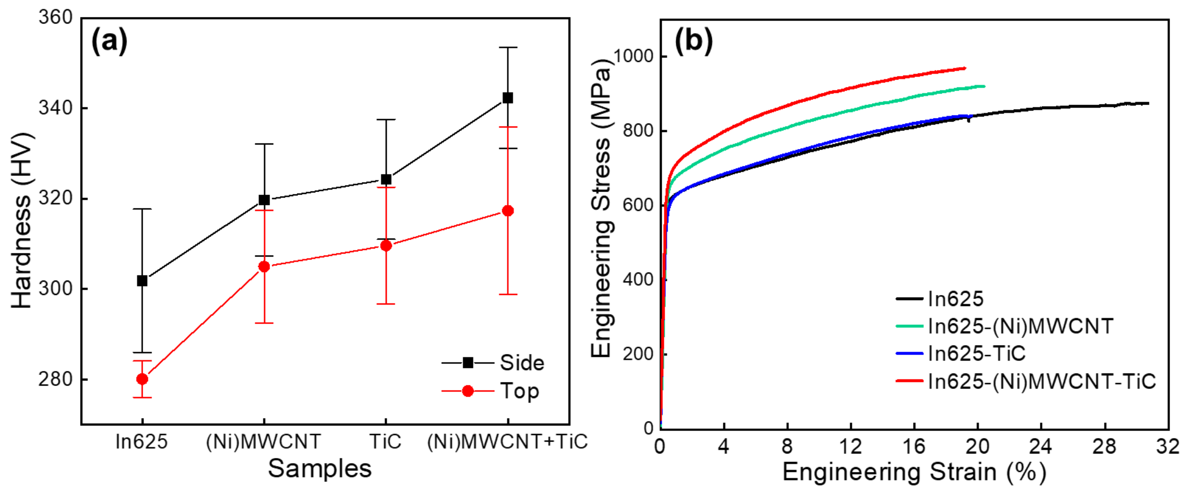

Figure 8. (a) Vickers hardness on the top and side planes of each sample; (b) the engineering stress-strain curves.

The effect of nano-additives on the yield strength is discussed below. Typically, the following mechanisms that resist dislocation motion in the alloy could contribute to the yield strength of it: the inherent lattice friction stress, solid solution strengthening, grain boundary strengthening (often described by the Hall-Petch relation), strengthening caused by higher dislocation densities, and secondary phase strengthening. Here in this study, as the nano-additives remain un-melted (due to their high melting temperature), the first two (friction stress and solid solution strengthening) should remain invariant in all the alloys. Given the change in grain size (obtained from EBSD), the difference in Hall-Petch strengthening can be estimated as $\Delta\sigma = k(d_1^{-0.5} - d_2^{-0.5})$, where k is the Hall-Petch coefficient and d is the grain size. Adopting k=750 MPa μm$^{-0.5}$ for IN625 from the literature [28], $\Delta\sigma$ (compared to IN625 sample without nano-additives) is calculated to be 9.2, 22.5, 7.6 MPa for IN625-(Ni)MWCNT, In625-TiC, and In625-(Ni)MWCNT-TiC, respectively. This result obviously cannot explain the enhancement of yield strength in IN625-(Ni)MWCNT (29.5 MPa) and IN625-(Ni)MWCNT-TiC (33 MPa).

The addition of nano-additives not only offers secondary phase strengthening, but also alters the melt pool characteristics during the fabrication process, which could lead to the variation of dislocation density and the formation of other phases (e.g., laves phase). As illustrated in Figure 6(e), incorporation of both (Ni)MWCNT and TiC resulted in finer cell size. In LPBF FCC samples, cellular structure and dislocation networks typically overlap [20,29], which means finer cell size leads to higher dislocation density and thus enhanced yield strength. Moreover, in MMCs, there are several other strengthening mechanisms, i.e., coefficient of thermal expansion mismatch, Orowan strengthening, and load-sharing (load-transfer), which involves volume fraction, aspect ratio, distribution, and interaction with dislocations of the additives/reinforcements [30]. Due to complexity of AM and the resultant microstructures, the empirical equations in the conventional MMCs cannot be readily applied. Future efforts will be devoted to this aspect.

Strain hardening behavior is closely related to ductility, as it facilitates the uniform plastic deformation and prevents stress concentration [31-33]. To understand the effect of nano-additives on strain hardening, the logarithmic true-stress/true-plastic-strain curves of each sample were plotted and shown in Figure 9. As can be seen, all samples exhibit two-stage strain hardening behavior (varying slop of the log-log plot), which is commonly seen in FCC metals due to the change of the mechanism in dislocation motion [34-36]. After fitting with Ludwik model $\sigma = K\varepsilon^n$, where K is material-related constants and n is work hardening exponent, the K and n of the two-stage plots were extracted and listed in Table 3. It is revealed that the n values in all the samples remain rather constant, indicating that the nano-additives did not significantly affect the strain hardening ability of the In625 alloy. Hence, the decrease in ductility is not induced by the variation of strain hardening ability.

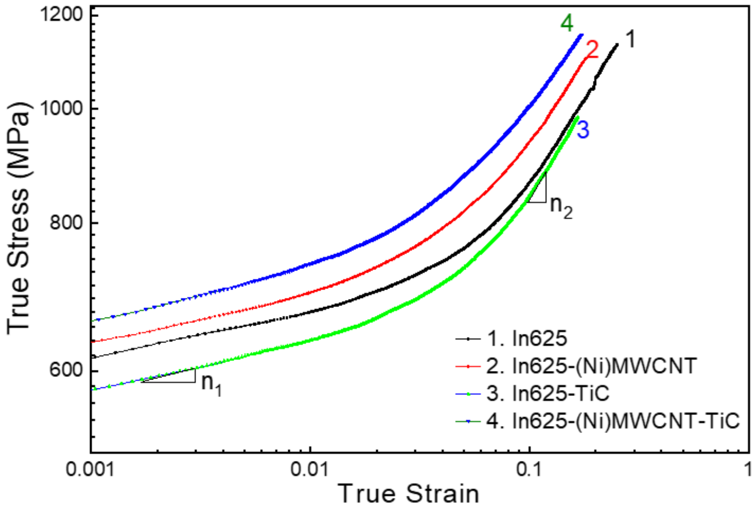

Figure 9. Logarithmic true-stress/true-plastic-strain plots of In625, In625-(Ni)MWCNT, In625-TiC, and In625-(Ni)MWCNT-TiC.

Table 3. Parameters obtained from the logarithmic true-stress/true-plastic-strain plots in Figure 9.

	Strain (0.001-0.01)		Strain (>0.1)	
	k1	n1	k2	n2
IN625	781.2717	0.03334	1692.929	0.2950
Ni/CNT-IN625	838.5886	0.04048	1749.849	0.2709
TiC-IN625	773.4938	0.04252	1692.629	0.3028
TiC-Ni/CNT-IN625	925.7685	0.04953	1824.514	0.2606

To further investigate the variation of ductility (Figure 8), the fracture surfaces of the tensile samples were characterized, as shown in Figure 10. It is observed that both dimples (indicating ductile fracture behavior) and quasi-cleavage (feature of brittle fracture) exist in all the samples. The quasi-cleavages features can be induced by the nano-additives, which are known to decrease the ductility and toughness of MMCs fabricated by conventional methods and AM [3,37]. Depending on the morphology and types of additives/reinforcement, their effects vary [37,38]. More specifically, when the matrix is particle-reinforced, the presence of particles imposes a constraint on the plastic deformation of the matrix, consequently causing substantial tensile hydrostatic stresses within the matrix. This leads to an increase in the load carried by the additives/reinforcements, consequently increasing the flow stress. However, it also leads to the premature occurrence of internal damage, manifesting as particle fracture, interface decohesion, and/or matrix void growth, resulting in the loss of ductility and toughness [37]. When the MMCs are reinforced by one-dimensional CNTs, the bonding between the CNTs and the matrix plays a significant role in affecting the ductility [39]. A robust bond between the CNTs and the matrix results in enhanced ductility due to fewer interfacial defects.

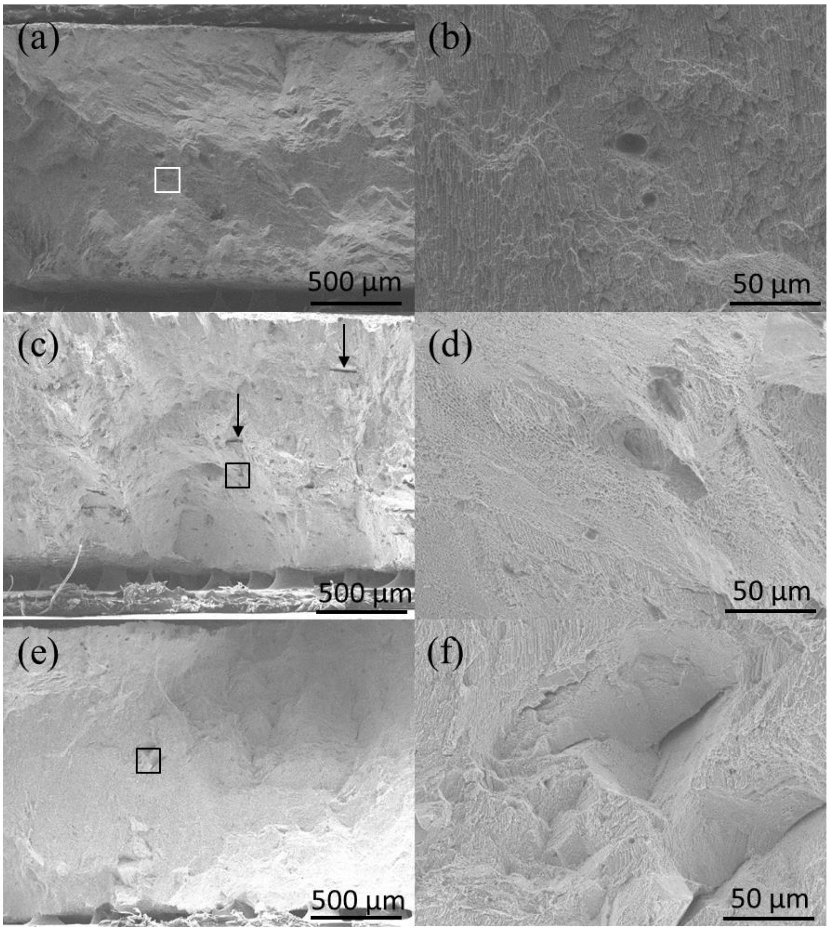

Figure 10. Fractography images of (a-b) In625-(Ni)MWCNT, (c-d) In625-TiC, and (e-f) IN625-(Ni)MWCNT-TiC. The boxes in (a), (c) and (e) indicate the magnified areas shown in (b), (d) and (f).

4. Conclusion

Two nano-additives, (Ni)MWCNT and TiC, were incorporated into In625 and four alloys were fabricated: In625, In625-(Ni)MWCNT, In625-TiC, and In625-(Ni)MWCNNT-TiC. The individual and collective effects of two nano-additives on the microstructure and mechanical properties were investigated and the major findings are listed below:

(1) Both nano-additives retained their structures after the fabrication process and were found to be locating along the boundaries of cellular structures. Collectively, the combination of (Ni)MWCNT and TiC results in finer cellular structures compared to their individual effects. The presence of tortuous boundaries in the cellular structures of the In625-(Ni)MWCNT-TiC sample indicates a substantial collective influence of nano-additives on dendrite growth.

(2) In contrast to samples containing either (Ni)MWCNT or TiC alone, the In625-(Ni)MWCNT-TiC sample exhibits enhanced hardness and strength. This can be credited to the combined effect of (Ni)MWCNT and TiC in refining the cellular structure, thereby potentially enhancing strengthening mechanisms such as dislocation density and load-sharing.

Since the fabrication of hybrid MMCs using AM techniques is still relatively unexplored, the discoveries in this study are believed to have broader applicability across various materials. These findings also offer insights into comprehending the individual and collective effects of nano-additives.

Acknowledgements

The authors gratefully appreciate the financial support from the Structural Metal Alloys Programme (Grant reference No.: A18B1b0061) from Agency for Science, Technology and Research of Singapore. The authors gratefully thank the technical assistance in selective laser melting from Dr Sing Swee Leong, Dr Tan Kok Ee and Dr Tan Hong Yi from the Additive Manufacturing Centre in Nanyang Technological University. The authors gratefully thank the technical assistance in tensile testing and EBSD data collection from Mr. Augustine Cheong and Dr Laura-Lynn Liew from Institute of Materials Research and Engineering, Agency for Science, Technology and Research of Singapore.

Data availability

The data that support the findings of this study are available from the corresponding author on reasonable request.

References

[1] J. H. Martin, B. D. Yahata, J. M. Hundley, J. A. Mayer, T. A. Schaedler, T. M. Pollock, 3D printing of high-strength aluminium alloys, Nature 549 (2017) 365-369.
[2] Q. Han, Y. Gu, R. Setchi, F. Lacan, R. Johnston, S. L. Evans, S. Yang, Additive manufacturing of high-strength crack-free Ni-based Hastelloy X superalloy, Additive Manufacturing 30 (2019) 100919.
[3] W. Zhai, Z. Zhu, W. Zhou, S. M. L. Nai, J. Wei, Selective laser melting of dispersed TiC particles strengthened 316L stainless steel, Composites Part B: Engineering 199 (2020).
[4] P. Wang, B. Zhang, C. C. Tan, S. Raghavan, Y.-F. Lim, C.-N. Sun, J. Wei, D. Chi, Microstructural characteristics and mechanical properties of carbon nanotube reinforced Inconel 625 parts fabricated by selective laser melting, Materials & Design 112 (2016) 290-299.
[5] J. Li, H. Qu, J. Bai, Grain boundary engineering during the laser powder bed fusion of TiC/316L stainless steel composites: New mechanism for forming TiC-induced special grain boundaries, Acta Materialia 226 (2022) 117605.
[6] G. Muvvala, D. Patra Karmakar, A. K. Nath, In-process detection of microstructural changes in laser cladding of in-situ Inconel 718/TiC metal matrix composite coating, Journal of Alloys and Compounds 740 (2018) 545-558.
[7] C. Hong, D. Gu, D. Dai, M. Alkhayat, W. Urban, P. Yuan, S. Cao, A. Gasser, A. Weisheit, I. Kelbassa, Laser additive manufacturing of ultrafine TiC particle reinforced Inconel 625 based composite parts: Tailored microstructures and enhanced performance, Materials Science and Engineering: A 635 (2015) 118-128.
[8] P. Jin, Y. Liu, F. Li, Q. Sun, Realization of synergistic enhancement for fracture strength and ductility by adding TiC particles in wire and arc additive manufacturing 2219 aluminium alloy, Composites Part B: Engineering 219 (2021) 108921.
[9] T. Zhao, M. Dahmen, W. Cai, M. Alkhayat, J. Schaible, P. Albus, C. Zhong, C. Hong, T. Biermann, H. Zhang, Laser metal deposition for additive manufacturing of AA5024 and nanoparticulate TiC modified AA5024 alloy composites prepared with balling milling process, Optics & Laser Technology 131 (2020) 106438.
[10] B. Zhang, G. Bi, Y. Chew, P. Wang, G. Ma, Y. Liu, S. K. Moon, Comparison of carbon-based reinforcement on laser aided additive manufacturing Inconel 625 composites, Applied Surface Science 490 (2019) 522-534.
[11] P. Wang, T. Li, Y.-F. Lim, C. K. I. Tan, D. Chi, Sintering and mechanical properties of mechanically milled Inconel 625 superalloy and its composite reinforced by carbon nanotube, Metal powder report 72 (2017) 271-275.
[12] D. Gu, X. Rao, D. Dai, C. Ma, L. Xi, K. Lin, Laser additive manufacturing of carbon nanotubes (CNTs) reinforced aluminum matrix nanocomposites: Processing optimization, microstructure evolution and mechanical properties, Additive Manufacturing 29 (2019) 100801.
[13] M. Y. Zhou, L. B. Ren, L. L. Fan, Y. W. X. Zhang, T. H. Lu, G. F. Quan, M. Gupta, Progress in research on hybrid metal matrix composites, Journal of Alloys and Compounds 838 (2020).
[14] Z. Li, G. Fan, Q. Guo, Z. Li, Y. Su, D. Zhang, Synergistic strengthening effect of graphene-carbon nanotube hybrid structure in aluminum matrix composites, Carbon 95 (2015) 419-427.
[15] B. Hekner, J. Myalski, N. Valle, A. Botor-Probierz, M. Sopicka-Lizer, J. Wieczorek, Friction and wear behavior of Al-SiC(n) hybrid composites with carbon addition, Composites Part B: Engineering 108 (2017) 291-300.
[16] J. Radhakrishnan, P. Kumar, S. Li, Y. Zhao, U. Ramamurty, Unnotched fatigue of Inconel 718 produced by laser beam-powder bed fusion at 25 and 600°C, Acta Materialia 225 (2022).
[17] A. N. D. Gasper, B. Szost, X. Wang, D. Johns, S. Sharma, A. T. Clare, I. A. Ashcroft, Spatter and oxide formation in laser powder bed fusion of Inconel 718, Additive Manufacturing 24 (2018) 446-456.
[18] M. S. Dresselhaus, A. Jorio, M. Hofmann, G. Dresselhaus, R. Saito, Perspectives on carbon nanotubes and graphene Raman spectroscopy, Nano Lett 10 (2010) 751-758.
[19] I. Calizo, A. Balandin, W. Bao, F. Miao, C. Lau, Temperature dependence of the Raman spectra of graphene and graphene multilayers, Nano letters 7 (2007) 2645-2649.
[20] S.-H. Li, Y. Zhao, J. Radhakrishnan, U. Ramamurty, A micropillar compression investigation into the plastic flow properties of additively manufactured alloys, Acta Materialia 240 (2022) 118290.

[21] S. Wei, P. Kumar, K. B. Lau, D. Wuu, L.-L. Liew, F. Wei, S. L. Teo, A. Cheong, C. K. Ng, B. Zhang, C. C. Tan, P. Wang, U. Ramamurty, Effect of heat treatment on the microstructure and mechanical properties of 2.4 GPa grade maraging steel fabricated by laser powder bed fusion, Additive Manufacturing 59 (2022) 103190.
[22] J. D. R. Selvam, I. Dinaharan, R. S. Rai. in *Encyclopedia of Materials: Composites* (ed Dermot Brabazon) 615-639 (Elsevier, 2021).
[23] T. DebRoy, H. L. Wei, J. S. Zuback, T. Mukherjee, J. W. Elmer, J. O. Milewski, A. M. Beese, A. Wilson-Heid, A. De, W. Zhang, Additive manufacturing of metallic components – Process, structure and properties, Progress in materials science 92 (2018) 112-224.
[24] L. Yao, S. Huang, U. Ramamurty, Z. Xiao, On the formation of "Fish-scale" morphology with curved grain interfacial microstructures during selective laser melting of dissimilar alloys, Acta Materialia 220 (2021) 117331.
[25] H. Yin, J. Yang, Y. Zhang, L. Crilly, R. L. Jackson, X. Lou, Carbon nanotube (CNT) reinforced 316L stainless steel composites made by laser powder bed fusion: Microstructure and wear response, Wear 496-497 (2022).
[26] S. Wei, K. B. Lau, J. J. Lee, F. Wei, W. H. Teh, B. Zhang, C. C. Tan, P. Wang, U. Ramamurty, Selective laser melting of Fe–Al alloys with simultaneous gradients in composition and microstructure, Materials Science and Engineering: A 821 (2021) 141608.
[27] N. C. Levkulich, S. L. Semiatin, J. E. Gockel, J. R. Middendorf, A. T. DeWald, N. W. Klingbeil, The effect of process parameters on residual stress evolution and distortion in the laser powder bed fusion of Ti-6Al-4V, Additive Manufacturing 28 (2019) 475-484.
[28] R. Kozar, A. Suzuki, W. Milligan, J. Schirra, M. Savage, T. Pollock, Strengthening mechanisms in polycrystalline multimodal nickel-base superalloys, Metallurgical and materials transactions A 40 (2009) 1588-1603.
[29] K. M. Bertsch, G. Meric de Bellefon, B. Kuehl, D. J. Thoma, Origin of dislocation structures in an additively manufactured austenitic stainless steel 316L, Acta Materialia 199 (2020) 19-33.
[30] Q. Li, S. Huang, Y. Zhao, Y. Gao, U. Ramamurty, Simultaneous enhancements of strength, ductility, and toughness in a TiB reinforced titanium matrix composite, Acta Materialia 254 (2023).
[31] D. K. Matlock, J. G. Speer. in *Microstructure and Texture in Steels: and Other Materials* 185-205 (Springer, 2009).
[32] K. O. Findley, J. Hidalgo, R. M. Huizenga, M. J. Santofimia, Controlling the work hardening of martensite to increase the strength/ductility balance in quenched and partitioned steels, Materials & Design 117 (2017) 248-256.
[33] S. Wei, C. Hutchinson, U. Ramamurty, Mesostructure engineering in additive manufacturing of alloys, Scripta Materialia 230 (2023) 115429.
[34] D. C. Ludwigson, Modified stress-strain relation for FCC metals and alloys, Metallurgical Transactions 2 (1971) 2825-2828.
[35] P. Kumar, R. Jayaraj, J. Suryawanshi, U. R. Satwik, J. McKinnell, U. Ramamurty, Fatigue strength of additively manufactured 316L austenitic stainless steel, Acta Materialia 199 (2020) 225-239.
[36] S. Wei, Y. Zhao, J.-i. Jang, U. Ramamurty, Rate-dependent mechanical behavior of single-, bi-, twinned-, and poly-crystals of CoCrFeNi high-entropy alloy, Journal of Materials Science & Technology 120 (2022) 253-264.
[37] A. Mortensen, J. Llorca, Metal Matrix Composites, Annual Review of Materials Research 40 (2010) 243-270.
[38] Q. Li, Y. Chen, X. Huang, Y. Wang, Y. Zhao, U. Ramamurty, Y. Gao, Long-whisker type TiB phase introduced by micron-sized precursors and its prominent strengthening effect in titanium matrix composites, Materials Science and Engineering: A 841 (2022).
[39] B. Chen, K. Kondoh, H. Imai, J. Umeda, M. Takahashi, Simultaneously enhancing strength and ductility of carbon nanotube/aluminum composites by improving bonding conditions, Scripta Materialia 113 (2016) 158-162.